PAPER

Elucidating decay pathways of bispidine–iron(IV)–tosylimido complexes: insights gained from decay products

Thomas Josephy,[a] Fridolin Röhs,[c] Thorsten Glaser,[c] Peter Comba [ID] [a,d] and Katharina Bleher [ID] *[a,b]

This study investigates the degradation pathways of three iron(IV)–tosylimido complexes coordinated by tetra- and pentadentate bispidine ligands, a class of rigid nitrogen-donor frameworks based on the 3,7-diazabicyclo[3.3.1]nonane scaffold. Using a combination of spectroscopic (UV-vis-NIR, EPR, Mössbauer) and spectrometric techniques (HR ESI-MS/MS) it was revealed that two of the complexes, derived from a tetradentate bispidine ligand and a pentadentate bispidine ligand, follow a common degradation route. This involves initial reduction to a high-spin iron(III) species, followed by ligand demethylation at a nitrogen donor. The demethylation step is confirmed by the elimination of a CH_2NTs (tosylaminomethyl) fragment, as detected by tandem mass spectrometry. This transformation is analogous to formaldehyde loss observed in the degradation of related bispidine-iron(IV)–oxido complexes. In contrast, an isomeric iron(IV)–tosylimido complex bearing a structurally similar pentadentate bispidine ligand follows a distinct pathway, forming a low-spin iron(III)–amido complex of the type **[(L)Fe–NHTs]²⁺**. Mössbauer parameters support this assignment and align with previously reported low-spin iron-amido species. We attribute the difference in reactivity to the orientation of the tosylimido group within the coordination sphere: axial in the isomeric pentadentate ligand, but equatorial in the other two. This spatial change influences both the electronic structure and the accessibility of the tosylimido moiety. Although direct observation of the transient iron(IV)–tosylimido intermediate remains elusive in the tetradentate system due to its high reactivity, analysis of its degradation products provides indirect but compelling evidence for its formation. All complexes mediate NTs transfer to styrene, supporting the presence of tosylimido intermediates and offering a platform for rational catalyst design through ligand and counter ion tuning.

Introduction

High-valent heme and nonheme metal–oxygen and metal–nitrogen complexes are powerful oxidants, playing pivotal roles in enzymatic transformations. These complexes have been extensively studied for their ability to transfer oxygen and nitrogen containing groups as fundamental reactions in both natural and synthetic chemistry.[1–6] Among these, nonheme iron–oxido species have been particularly well characterized, with diverse examples spanning multiple oxidation and spin states, as well as other catalytically active oxygen containing species such as superoxido and peroxide complexes.[7–12] These studies have laid a strong foundation for understanding structure–reactivity relationships in iron–oxido chemistry through kinetic, spectroscopic, and quantum-chemical approaches. Since the early 2000s iron–imido complexes have gained increasing interest; however, detailed insight into their structural, spectroscopic, and mechanistic properties remains limited.[13–18]

Iron–imido species, in particular iron(IV)–tosylimido complexes, hold great potential for nitrene transfer chemistry, including aziridination and amination of hydrocarbons, offering promising routes for C–N bond formation.[19–21] Such transformations are critical in the synthesis of nitrogen-containing molecules with applications ranging from pharmaceuticals[22,23] to advanced materials.[24] Studies involving among others copper,[25–31] manganese,[32,33] and iron complexes[34,35] have demonstrated the utility of metal–imido systems for nitrene transfer. Spectroscopically characterized examples have been widely reported and comparisons of reactivity with the well-studied iron–oxido species suggest intriguing differences.[35–39] Typically, iron–tosylimido complexes

[a]*Universität Heidelberg, Anorganisch-Chemisches Institut, INF 270, D-69120 Heidelberg, Germany. E-mail: Katharina.bleher@kit.edu*
[b]*Institute of Functional Interfaces, Karlsruhe Institute of Technology, Hermann-von-Helmholtz-Platz 1, 76344 Eggenstein-Leopoldshafen, Germany*
[c]*Universität Bielefeld, Lehrstuhl für Anorganische Chemie I, Fakultät für Chemie, Universitätsstr. 25, D-33615 Bielefeld, Germany*
[d]*Universität Heidelberg, Interdisziplinäres Zentrum für Wissenschaftliches Rechnen (IWR), Germany*

are orders of magnitude slower in group transfer reactions and exhibit slower rates for hydrogen atom transfer (HAT) compared to their oxido counterparts. However, iron(IV)–tosylimido complexes can show enhanced reactivity in certain sulfoxidation reactions, attributed to differences in electron transfer properties and sterics.[20,40]

In general, the observed reactivity is sufficient to trigger various decomposition processes, similar to the formation of iron(III)–hydroxido compounds or N-centered demethylation of the used ligand as seen in oxido analogs.[41–43] It has been shown that tosylimido groups can form [Fe–NHTs] species via proton coupled electron transfer (see Scheme 1, pathway B).[34] These species are likewise capable of transferring the amine group, thereby aminating the respective substrate instead of forming a nitrene or aziridine.[44,45] Furthermore, the tosylimido group, as seen in many cases of oxido chemistry, can attack its own ligand, triggering an intramolecular rearrangement (Scheme 1, pathway A).[14] Due to this, acquiring iron(IV)–tosylimido spectra without any impurities is often challenging, as many of these decay processes occur immediately upon the oxidation of the precursor.

Recently, iron(IV)–tosylimido complexes supported by the two isomeric pentadentate bispidine ligands L^2 and L^3 (see Fig. 1 for all used ligands in this manuscript and their complex structures) have been reported and characterized.[40] In contrast, no spectroscopic data are available for the tosylimido species of the tetradentate ligand L^1. The absence of experimental evidence for the L^1-bound tosylimido complex is attributed to an enhanced decay rate of the tosylimido intermediate, preventing its direct detection. On the basis of the exceptionally high reactivity of the iron(IV)–oxido complex with L^1, it was hypothesized that the L^1-supported tosylimido species might likewise exhibit increased reactivity compared to other tosylimido species.[41] To probe this, we conducted experiments aimed at identifying the elusive iron(IV)–tosylimido intermediate and elucidating its decay pathways. Our strategy involved a comparative study of the L^1-based system alongside the pre-

viously characterized L^2 and L^3 complexes to establish whether the same decomposition products are observed across all three ligands. Such a correlation would support the formation of a common reactive intermediate. Herein, we report our findings based on HR ESI-MS, UV-vis-NIR, Mössbauer, and EPR spectroscopy, complemented by catalytic aziridination reactions using styrene as substrate.

Results and discussion

Characterization of the decay species

UV-vis-NIR spectroscopy. The combination of various spectroscopic methods is often required to fully characterize a reactive species or its degradation products. Accordingly, a combination of methods was employed in this study to capture the nature of the observed degradation products formed from bispidine-iron(IV)–tosylimido species. A commonly used method to observe the formation of reactive species of transition metal complexes is UV-vis-NIR spectroscopy. When a solution of the complexes of the pentadentate bispidines $[(L^2)Fe^{II}(MeCN)](OTf)_2$ and $[(L^3)Fe^{II}(MeCN)](OTf)_2$ (0.5 mM, dry MeCN, Ar) are treated with 3 equivalents of the oxidizing agent PhINTs ((N-(p-toluenesulfonyl)imino)phenyliodinane), the formation of the tosylimido species can be observed by monitoring the corresponding absorption bands, see Fig. 2a and c. The tosylimido species for $[(L^{2/3})Fe^{IV}=NTs]^{2+}$ exhibit the same dd transitions at 735 nm or 730 nm, respectively, as known for their oxido analogues. The maxima are not shifted as the involved orbitals of this transition are not directly influenced by the coordinating oxido or tosylimido group.[40,46] Additionally, the tosylimido species $[(L^3)Fe^{IV}=NTs]^{2+}$ shows an intense charge-transfer band at 475 nm, as also reported for the tosylimido complex $[(L^6)Fe^{IV}=NTs]^{2+}$.[35] When the solutions are left to stand, the corresponding tosylimido bands of both complexes decrease as the tosylimido species transform into decay products, which do not correspond to the iron(II) precursor but to iron(III) species, with bands at 530 nm or 500 nm, respectively. The time for the complete decay of the corresponding tosylimido bands differs significantly, ranging from a few minutes to several hours.

In Fig. 2a the time-dependent spectra of the oxidation process of $[(L^2)Fe^{II}(MeCN)]^{2+}$ to the corresponding tosylimido complex and the subsequent decay process are shown. The close-up depicts the isosbestic point associated with the decay process, indicating that the resulting iron(III) species originates from the transformation of the iron(IV)–tosylimido species. The time traces at 780 nm for the tosylimido band and at 530 nm for the decay species are shown in Fig. 2b to illustrate the temporal progression of the decay.† In Fig. 2c, the oxidation to the tosylimido species and subsequent decay are illustrated for the
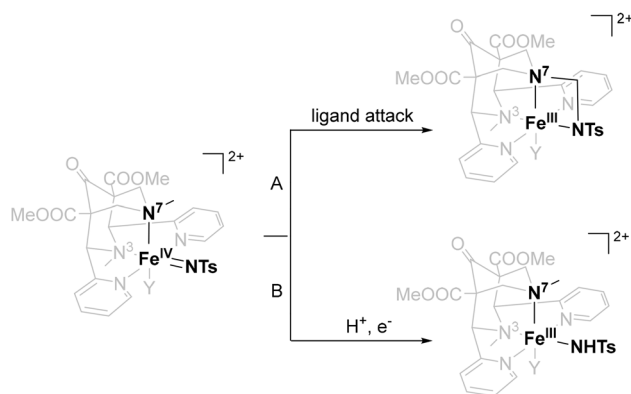
Scheme 1 Observed decomposition pathways of iron(IV)–tosylimido species, exemplarily shown on a complex with a tetradentate bispidine ligand.

---

† For the time trace the absorption at 780 nm was chosen, although the absorption maximum is at 730 nm, as no absorption of the charge transfer band is observed at 780 nm and thus the progression of the dd absorption can be more clearly represented.
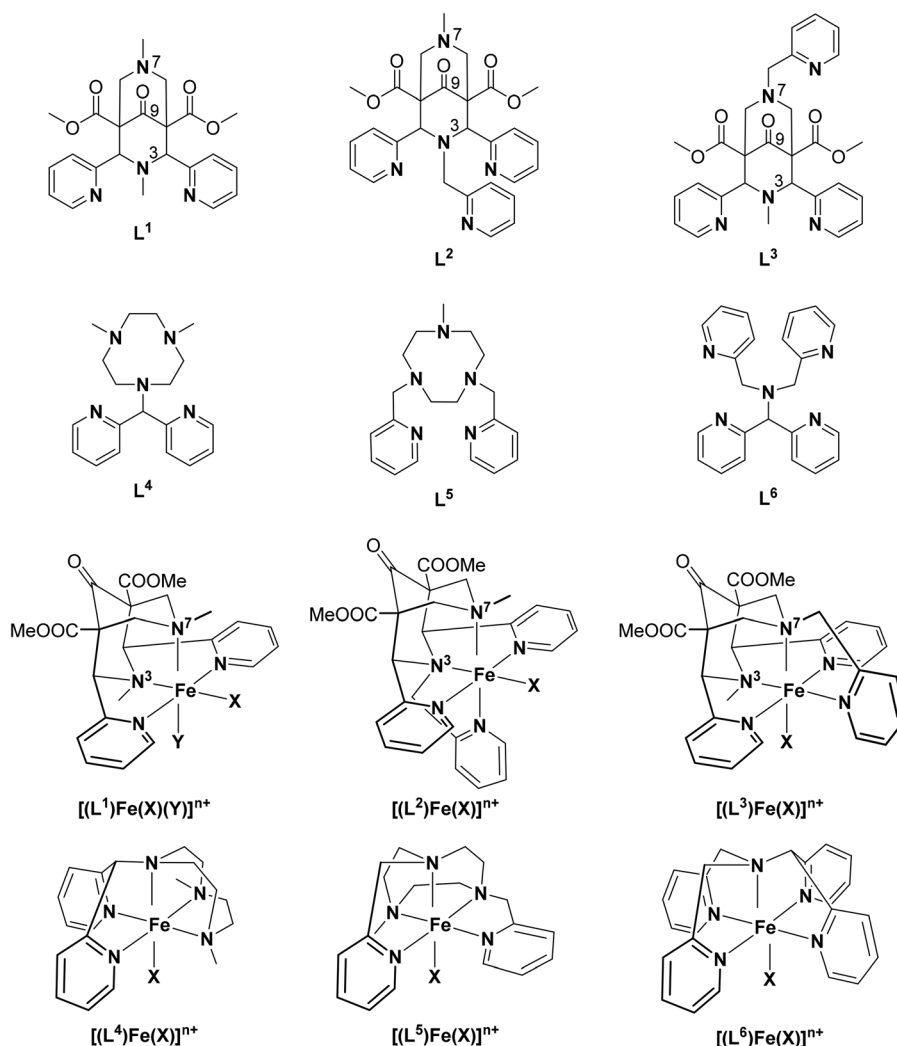
Fig. 1 Illustration of the ligands and complexes mentioned in the manuscript. For the complexes, X and Y are either a solvent molecule, anion or the tosylimido group.

complex with L^3, where the changes in the spectrum are relatively minor due to the charge transfer band of the tosylimido complex. Here, a shift of the charge transfer band from 475 nm to 500 nm is observed.

When $[(L^1)Fe^{II}(Cl)_2]$ or $[(L^1)Fe^{II}(MeCN)_2](OTf)_2$ are reacted with 3 equivalents of PhINTs, no transitions typical for high-valent iron(IV) species are observed. Instead, an intense charge transfer band around 500 nm or 480 nm is observed, depending on whether OTf^- or Cl^- are used as counter ion (see SI Fig. S1 and S2 for time-dependent UV-vis-NIR spectra). An overview of the resulting iron(III) bands for all bispidine-iron complexes is shown in Fig. 2d. It is noteworthy that the iron(III) bands of the degradation products of the assumed $[(L^1)Fe^{IV}=NTs]^{2+}$ species, independent of the coligand, and of $[(L^2)Fe^{IV}=NTs]^{2+}$ remain stable for several hours or days, while the iron(III) band of the degradation product of $[(L^3)Fe^{IV}=NTs]^{2+}$ further decays within approximately 2 hours.

Mass spectrometry

Various studies have shown that high-valent iron–tosylimido species often undergo decay via protonation of the tosylimido moiety and subsequent reduction of the iron(IV) center to iron(III), resulting in the formation of an $[Fe^{III}–NHTs]$ species.[34,47–49] Such species have, for example, been characterized in systems supported by the ligands L^4 and L^5. Additionally, it is known that intramolecular group attack can occur in bispidine-based systems as well as in other non-heme model complexes, leading to the degradation of the reactive species involving N-centered demethylation.[41,42,50] To further investigate the degradation products of the three bispidine-based iron(IV)–tosylimido complexes, we analyzed them by high-resolution electrospray ionization mass spectrometry (HR ESI-MS) and tandem MS. An overview of the key species found in the collected spectrometric data for all complexes is provided in Table 1 (see SI Fig. S9–S20 for a complete set of
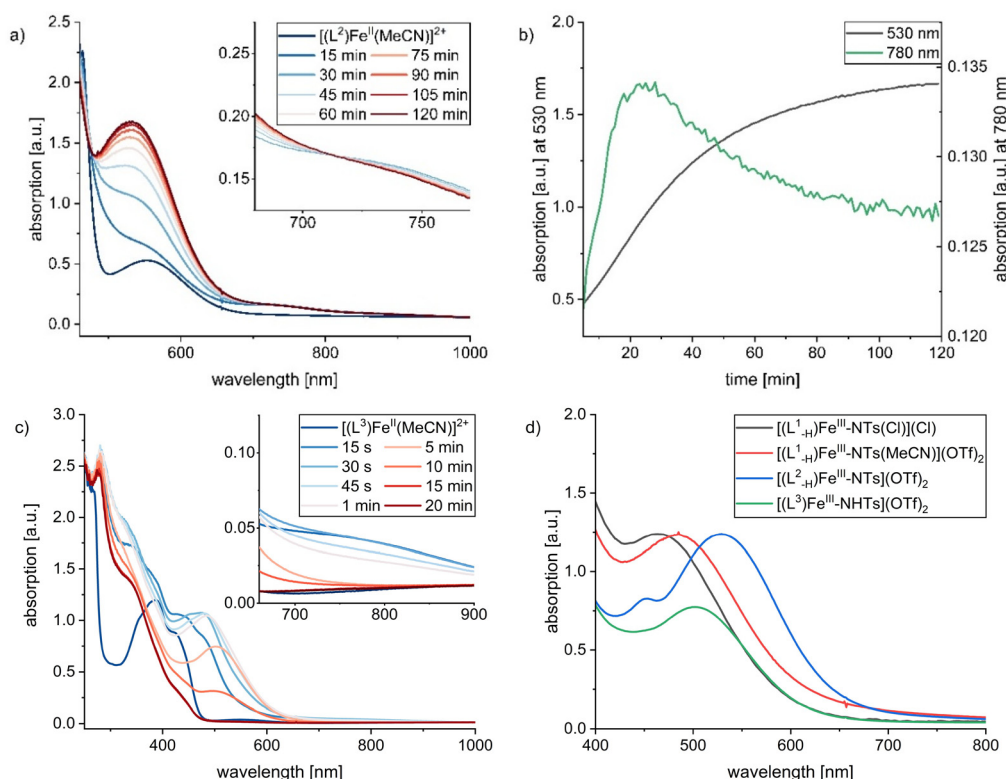
Fig. 2 (a) Time-dependent progression of the oxidation of $[(L^2)Fe^{II}(MeCN)]^{2+}$ to the tosylimido species and its subsequent decay; the insert shows the isosbestic point observed during the decay of the tosylimido species. (b) Time-dependent progression of the absorptions at 780 nm (for the iron(IV)−tosylimido species; maximum at 735 nm) and 530 nm (decay product) for $[(L^2)Fe^{IV}\!\!=\!\!NTs]^{2+}$. (c) Time-dependent progression of the oxidation of $[(L^3)Fe^{II}(MeCN)]^{2+}$ to the tosylimido species and its subsequent decay. (d) Overview of all resulting iron(III) degradation products after oxidation with PhINTs. Resulting structures were determined using the combination of experiments shown below, which was the main finding of this study. All UV-vis-NIR spectra were recorded using an $[(L)Fe^{II}(X)_n]^{m+}$ concentration of 0.5 mM in MeCN, and 3 eq. PhINTs, measurements were carried out under Ar at rt.

Table 1 Most prominent decay species identified *via* HR ESI-MS after different aging times. Sample solutions (0.5 mM in MeCN) were stirred for a given time interval at rt after addition of 1–2 eq. PhINTs. Subsequently, the solutions were diluted to concentrations of 10^{-5} M and then measured

| Complex	Species	Sum formula	Mass m/z	1 min Int [%]	30 mi Int [%]	1 h Int [%]	5 h Int [%]	24 h Int [%]
$[(L^1)Fe^{II}(MeCN)_2](OTf)_2$	$[(L^1_{-H})Fe^{III}-NTs]^+$ (A*)^a	$C_{30}H_{32}FeN_5O_7S^+$	662.1366	16.2			100	100
	$[(L^1_{-CH_3})Fe^{III}-NTs]^+$ (B*)	$C_{29}H_{30}FeN_5O_7S^+$	648.1215	5.7			0.6	0.5
	$[(L^1_{-H})Fe^{III}-NTs]^{2+}$ + OH$^-$ (A)	$C_{30}H_{33}FeN_5O_8S^+$	679.1394	100			75	87.5
$[(L^1)Fe^{II}Cl_2]$	$[(L^1_{-H})Fe^{III}-NTs]^+$ (A*)	$C_{30}H_{33}FeN_5O_7S^+$	662.1366	30.9			100	100
	$[(L^1_{-H})Fe^{III}-NTs]^{2+}$ + Cl$^-$ (A)	$C_{30}H_{32}ClFeN_5O_7S^+$	697.1055	100			28.1	86.9
$[(L^2)Fe^{II}(MeCN)](OTf)_2$	$[(L^2_{-H})Fe^{III}-NTs]^{2+}$ + MeO$^-$ (A)	$C_{36}H_{38}FeN_6O_8S^+$	770.1816			100	100	
	$[(L^2_{-CH_3})Fe^{III}]^{2+}$ + OTf$^-$ (B)	$C_{28}H_{26}F_3FeN_5O_8S^+$	705.0798			22	14	
	$[(L^2_{-CH_2})Fe^{III}]^{2+}$ + OTf$^-$ (B)	$C_{28}H_{27}F_3FeN_5O_8S^+$	706.0876				27	
$[(L^3)Fe^{II}(MeCN)](OTf)_2$	$[(L^3)Fe^{III}-NTs]^+$ (E)	$C_{35}H_{36}FeN_6O_7S^+$	740.1710	79.1	100			
	$[(L^3)Fe^{III}-NTs]^{2+}$ + OTf$^-$ (E*)	$C_{36}H_{36}FeF_3N_6O_{10}S_2^+$	889.1230	3.2	8.8		12.0	5.1

^{a} The HR ESI-MS shows species **A**, **B** and **E** with charges of 1+ and 2+. The observation of the one-electron reduced or oxidized species is not unusual for transition metal complexes with reactive nitrogen ligands such as tosylamide, since these tend to undergo facile reduction or oxidation. Redox processes induced by HR ESI-MS is indicated by an asterisk (*).[40,42,51,53]

spectra and Table S1 for a detailed list of all species identified).

First the spectra of the oxidized tetradentate iron complexes with different counter ions were examined with HR ESI-MS. Both complexes show similar signals to those of the corres-ponding iron(IV)–oxido complexes.[41,42] In the HR ESI-MS spectra, the dominant signal corresponds to a species reduced by one proton and one electron, formally a hydrogen atom (Scheme 2, species **A**). This species remains the main component for up to 24 hours. To confirm the proposed degra-
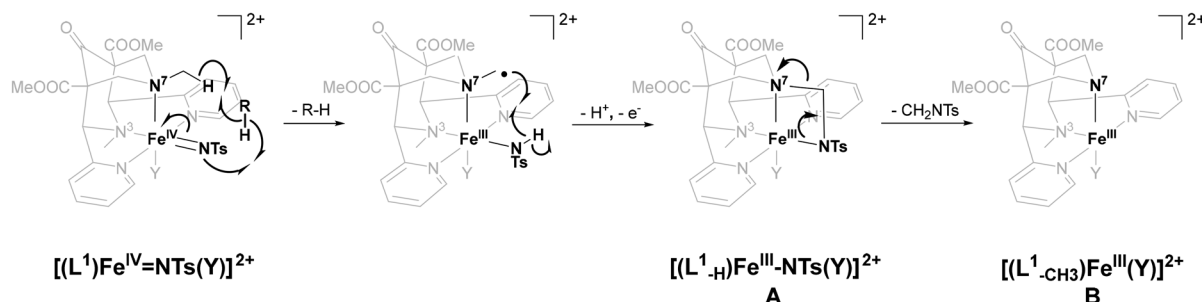
Scheme 2 Postulated decay pathways of the iron(IV)–tosylimido species with bispidine ligands L^1 and L^2, Y is either a counter ion, solvent molecule or the pendant pyridine from the ligand. R–H is a sacrificial solvent molecule, which mediates the decay pathway.

dation pathway for the tosylimido complex, tandem-MS experiments were performed on the $[(L^1_{-H})Fe^{III}–NTs]^+$ ion (Fig. 3, see SI Fig. S8 for different acceleration voltages). The spectra shows elimination of a CH_2NTs fragment, consistent with demethylation of the ligand. This cleavage is mechanistically analogous to the loss of formaldehyde observed in the degradation of the corresponding oxido species (see Scheme 2), suggesting a shared degradation route for the iron(IV)–oxido and –tosylimido complexes supported by L^1. UV-vis-NIR spectroscopy also supports the formation of $[(L^1_{-H})Fe^{III}–NTs]^{2+}$ (A). For the OTf^- complex, an absorption band at 500 nm is observed (480 nm for Cl^-), which remains stable over time. Species **A** can further degrade via CH_2NTs elimination to give species **B** (Scheme 2), although only trace amounts of **B** are detected by HR ESI-MS. The consistency between the dominant MS species and the persistent UV-vis-NIR signal supports the assignment of species **A** as the primary degradation product.

The complex $[(L^2)Fe^{IV}=NTs]^{2+}$ follows the same degradation pathway as its L^1 analogue. In HR ESI-MS spectra, species with cleaved methyl groups appear around 60 minutes after oxidation (see Table 1), consistent with the demethylation mechanism outlined in Scheme 2. UV-vis-NIR spectroscopy

supports this assignment: an iron(III) species with an absorption band at 530 nm is observed, which decays further over time (see SI Fig. S7). Although the demethylation might proceed via an intramolecular pathway and thus be concentration-independent, the observed lifetime of $[(L^2)Fe^{IV}=NTs]^{2+}$ varies significantly, from hours to several days, across experiments. This variability suggests that hydrogen atom transfer (HAT) involving the solvent or medium contributes to the decay mechanism (see Scheme 2). In this context, the solvent may act as a formal hydrogen donor. Analogous behavior has been reported for related iron–tosylimido complexes with tripodal urea- or amide-based ligands (L^4, L^5), where the $[Fe^{IV}=NR]$ species is reduced to $[Fe^{III}–NHR]$ via solvent-mediated HAT.[34,38,52] Moreover, the presence of water accelerates this transformation, as the resulting iron(III)–amido intermediate is rapidly protonated to yield an $[Fe^{III}–OH]$ complex.[34,38,52] Such a protonation-induced decay is consistent with the transient nature of $[(L^2)Fe^{IV}=NTs]^{2+}$ and highlights the extreme sensitivity of $[Fe^{IV}=NR]$ species to protic impurities. Notably, the analogous oxido complex $[(L^2)Fe^{IV}=O]^{2+}$ shows no signs of demethylation (see SI Fig. S6, S23 and S24).

No demethylation products were detected for $[(L^3)Fe^{IV}=NTs]^{2+}$ in HR ESI-MS. Interestingly, although the corresponding oxido
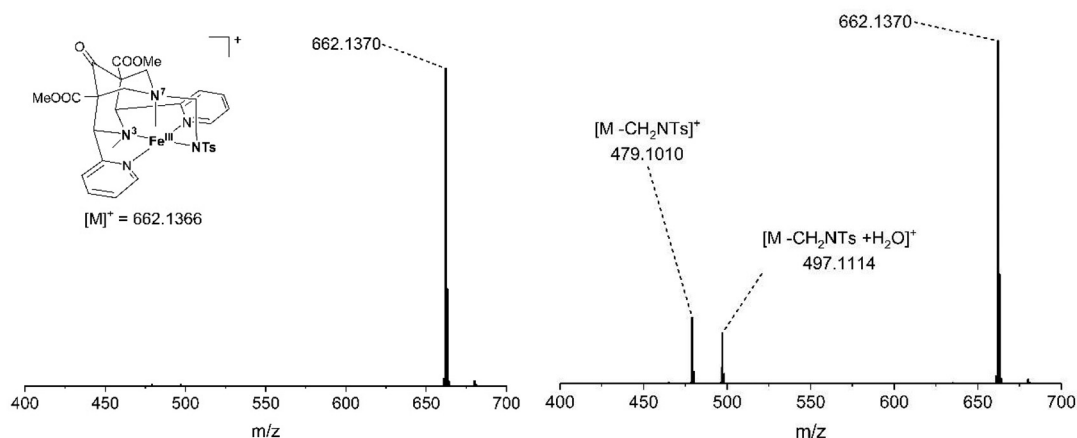

Fig. 3 Tandem HR ESI-MS measurement of the degradation product $[(L^1_{-H})Fe^{III}NTs]^+$ (M, species A*). Isolated species (left) and fragmentation products ([M-CH$_2$NTs]$^+$, species B*) at 15 V acceleration voltage (right).

complex $[(L^3)Fe^{IV}=O]^{2+}$ shows N-centred demethylation (see SI Fig. S21 and S22), the tosylimido complex yields a persistent signal at m/z 740.1710, assigned to $[(L^3)Fe^{III}-NTs]^+$. This species reaches maximum intensity around 30 minutes after oxidation (see SI Table S1 and Fig. S9–S20). To determine whether the species observed at m/z 740.1710 represents the intact $[(L^3)Fe^{IV}=NTs]^{2+}$ complex or a degradation product, a solution of the iron–tosylimido complex was monitored by UV-vis-NIR spectroscopy until the characteristic bands of $[(L^3)Fe^{IV}=NTs]^{2+}$ completely vanished (see SI Fig. S3 and S17). HR ESI-MS analysis of the fully decayed solution still showed the m/z 740.1710 peak, indicating that this is not the intact iron(IV)–tosylimido complex, but a more stable decay product. Further HR ESI-MS measurements confirmed that once the charge-transfer band of this species also disappeared (SI Fig. S4 and S19), the signal at m/z 740.1710 was no longer detectable. These findings suggest that $[(L^3)Fe^{III}-NHTs]^{2+}$ is the main degradation product of $[(L^3)Fe^{IV}=NTs]^{2+}$. Under HR ESI-MS conditions, the $[(L^3)Fe^{III}-NHTs]^{2+}$ species (D, Scheme 3) likely deprotonates at the NHTs group, yielding the corresponding singly charged $[(L^3)Fe^{III}-NTs]^+$ ion E.[54] Similar degradation pathways have been reported for related complexes with ligands L^4 and L^5.[34] The formation of this decay product could also explain the varying formation rates. As proposed for the L^1- and L^2-based complexes, where substrate-mediated hydrogen atom transfer plays a role in tosylimido reduction, the degradation rate of $[(L^3)Fe^{IV}=NTs]^{2+}$ likewise appears to depend on the availability of H-donors. To probe this, 10 mM (20 eq.) of 1,3-cyclohexadiene, a reagent with a

relatively low HAT barrier, was added to a solution of $[(L^3)Fe^{IV}=NTs]^{2+}$. Upon addition, the charge-transfer band immediately shifted from 475 nm to 530 nm, consistent with a rapid conversion into the $[(L^3)Fe^{III}-NHTs]^{2+}$ species (see SI Fig. S5). Interestingly, despite the presence of excess 1,3-cyclohexadiene, no second HAT was observed that would yield an NH_2Ts group and an iron(II) species, suggesting high stability of $[(L^3)Fe^{III}-NHTs]^{2+}$. The initially formed 1,3-cyclohexadienyl radical can either recombine, undergo disproportionation to form benzene and cyclohexene, or react with another equivalent of $[(L^3)Fe^{IV}=NTs]^{2+}$, ultimately leading to its conversion into benzene.[48,55,56] The degradation pathways of $[(L^3)Fe^{IV}=NTs]^{2+}$ are summarized in Scheme 3. In this scheme, 1,3-cyclohexadiene mediates HAT to generate the $[Fe^{III}-NHTs]^{2+}$ species (species D), which subsequently loses a proton under HR ESI-MS conditions to form the observed species E (m/z 740.1710). Alternatively, cleavage of the NHTs ligand (species F) yields iron(III) or iron(II) species, both of which are also detected by HR ESI-MS and UV-vis-NIR spectroscopy.

The isomeric pentadentate bispidine ligands L^2 and L^3 display complementary reactivity patterns in their corresponding iron(IV)–oxido and –tosylimido complexes with respect to N-centered demethylation. While $[(L^3)Fe^{IV}=O]^{2+}$ undergoes demethylation, the analogous $[(L^3)Fe^{IV}=NTs]^{2+}$ complex stops at hydrogen atom transfer from a sacrificial substrate, yielding a protonated tosylamide. Conversely, $[(L^2)Fe^{IV}=O]^{2+}$ remains inert toward demethylation, whereas $[(L^2)Fe^{IV}=NTs]^{2+}$ induces formal C–N bond cleavage. These
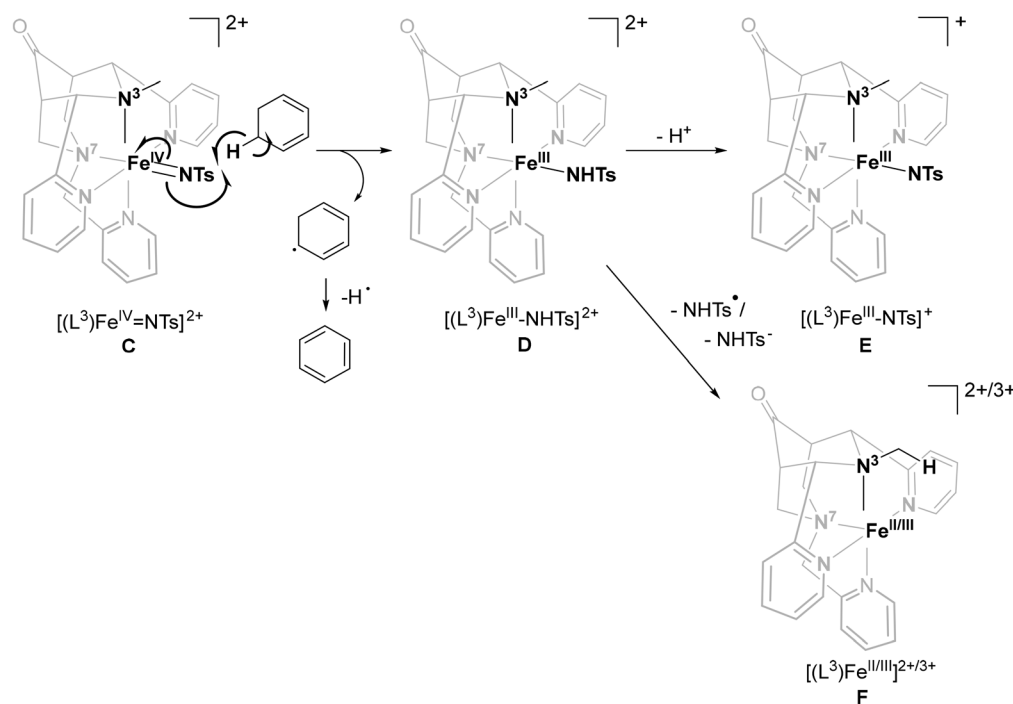
Scheme 3 Decay pathways for the complex $[L^3Fe^{IV}=NTs]^{2+}$ with 1,3-cyclohexadiene as sacrificial substrate. As proposed before, water or solvent molecules can also act as sacrificial substrate when no additional 1,3-cyclohexadiene is added.[34,47]

contrasting behaviors arise from a combination of complex geometry and intrinsic oxidant properties. The oxido ligand in $[(L^2)Fe^{IV}=O]^{2+}$ is well stabilized by the ligand field and remains unreactive toward the adjacent N–CH₃ group.[57] In the tosylimido analogue $[(L^2)Fe^{IV}=NTs]^{2+}$, however, the bulkier and electronically distinct NTs group experiences greater steric strain, which not only enhances its general reactivity, as seen in tosylimido atom transfer reactions,[40] but also facilitates intramolecular demethylation via HAT and subsequent C–N bond cleavage. In the case of L^3-based complexes, the situation is reversed. The Fe^{IV}=O moiety in $[(L^3)Fe^{IV}=O]^{2+}$ is sufficiently basic and accessible to abstract a hydrogen atom from the ligand's N–CH₃ group, thereby initiating demethylation. The corresponding tosylimido complex $[(L^3)Fe^{IV}=NTs]^{2+}$, though capable of HAT, does not proceed beyond formation of a protonated tosylamide. Previous density functional theory calculations (DFT) show that, for the two pentadentate tosylimido species, equatorial coordination of the NTs group leads to a larger Fe–N–S angle than axial coordination (150° vs. 140°).[40] This more linear arrangement decreases the σ overlap of Fe $d_{x^2-y^2}$ and enhances the π overlap of d_{xz}/d_{xy} with N p orbitals, thereby increasing the multiple-bond character of the Fe=NTs unit.[18] The stronger π bond with the NTs group decreases the stability of the lone pair at the nitrogen and thus increases the reactivity towards ligand self-decay. In contrast, the more bent arrangement (≈140°) in the axial case leads to a weaker orbital overlap resulting in reduced π interaction, making self-decay less favorable. Accordingly, in $[(L^2)Fe^{IV}=NTs]^{2+}$ geometric and electronic factors appear to stabilize the transient α-amino radical formed after HAT and thus enable C–N bond cleavage, whereas in $[(L^3)Fe^{IV}=NTs]^{2+}$ the same intermediate is kinetically trapped, either due to a less favorable in-plane approach geometry or an insufficient driving force for bond scission, so that no complete degradation occurs. To further support the hypothesis of different decay pathways, EPR and Mössbauer spectra were recorded to further characterize the various species.

Mössbauer and EPR spectroscopy

After identifying $[(L^3)Fe^{III}–NHTs]^{2+}$ (species **D** Scheme 3) and $[(L^{1/2}_{-H})Fe^{III}–NTs]^{2+}$ (species **A** Scheme 2) as the primary decay product of their respective tosylimido-complexes, the resulting iron(III) complexes were further characterized by EPR and Mössbauer spectroscopy. The Mössbauer samples were prepared by allowing the solutions of oxidized iron complex to age for 10–90 minutes, followed by rapid freezing in Teflon cups placed on a nitrogen-cooled metal block. At this point, corresponding to the MS data, the $[(L^{1/2}_{-H})Fe^{III}–NTs]^{2+}$ and $[(L^3)Fe^{III}–NHTs]^{2+}$ species are expected to be dominant species. First, the spectra of $[(L^{1/2}_{-H})Fe^{III}–NTs]^{2+}$ are examined. The Mössbauer spectra of both $[(L^1_{-H})Fe^{III}–NTs]^{2+}$ and $[(L^2_{-H})Fe^{III}–NTs]^{2+}$ exhibit signatures consistent with high-spin ferric centers (see Fig. 4a–c). For comparison, Mössbauer parameters and EPR data for the most important species are summarized in Table 2. All three complexes display identical isomer shifts of $\delta = 0.48$ mm s^{-1}, differing only in their quad-

rupole splittings: ΔE_Q = 1.19, 0.83 and 0.59 mm s^{-1}, for $[(L^1_{-H})Fe^{III}–NTs(Cl)](Cl)$, $[(L^1_{-H})Fe^{III}–NTs(MeCN)](OTf)_2$ and $[(L^2_{-H})Fe^{III}–NTs](OTf)_2$, respectively. The uniform isomer shifts and minor ΔE_Q differences corroborate the common degradation mechanism. In addition to the expected high-spin iron(III) species associated with $[(L^{1/2}_{-H})Fe^{III}–NTs]^{2+}$ (species **A** in Scheme 2),[41,42] an additional high-spin iron(III) signal appears in the Mössbauer spectra of the decayed $[(L^1)Fe^{IV}=NTs(MeCN)](OTf)_2$, which is absent in the others.

To gain further insight, EPR spectra were recorded (Fig. 4a–c). Samples of the L^1-based complexes were measured 5 h and of L^2-based complexes 24 h after oxidation to ensure strong signals of $[(L^{1/2}_{-H})Fe^{III}–NTs]^{2+}$. In addition to the expected high-spin signal, a low-spin iron(III) species was also detected for the triflate complexes (L^1 and L^2), with particularly strong intensity for the L^1 derivative. These low-spin features are absent in the corresponding chloride complex and are not reflected in the Mössbauer spectra, likely due to the higher measurement temperature (80 K vs. 8–12 K in EPR), which favors the high-spin state. The observation aligns with known temperature-dependent spin equilibria in bispidine-based iron(III) complexes.[58] The tendency of the triflate derivatives to form low-spin species is attributed to MeCN coordination, which is favored in the absence of strongly coordinating anions like chloride.

Based on the MS, EPR, and Mössbauer data, it is assumed that the additional high-spin iron(III) signal observed in the Mössbauer spectrum of $[(L^1_{-H})Fe^{III}–NTs(MeCN)](OTf)_2$ arises from ligand exchange of the –CH₂NTs group. This group appears to be labile and readily replaceable, a process that is suppressed in the corresponding chloride complex due to coordination of the chloride anion, and in the pentadentate ligand complex due to the altered ligand field. Supporting this interpretation, UV-vis-NIR data also show a slower decay of the degradation product when chloride is present (see SI Fig. S1 and S2), consistent with a reduced rate of –CH₂NTs dissociation. Ligand exchange may be triggered, for instance, during the freezing step of the Mössbauer sample preparation, as this was performed outside the glovebox. Under such conditions, moisture may condense into the sample during cooling and lead to exchange to an aqua or hydroxido ligand. This assignment is consistent with previous DFT calculations on analogous oxido complexes, which showed that Fe–CH₂O bonds are relatively weak and prone to dissociation,[41] as well as previous studies who reported a fast ligand exchange with traces of water.[52] It is therefore plausible that the Fe–CH₂NTs bond in the current system is similarly labile.

For the complex derived from L^3, the data point to a distinct degradation pathway involving formation of an $[(L^3)Fe^{III}–NHTs]^{2+}$ species. This is reflected in the Mössbauer spectrum (Fig. 4d), which, unlike the spectra of the L^1- and L^2-derived complexes, is dominated by a low-spin iron(III) species with an isomer shift of $\delta = 0.32$ mm s^{-1} and a quadrupole splitting of $\Delta E_Q = 2.28$ mm s^{-1}. These parameters are consistent with previously reported $[(L^{4/5})Fe–NHTs]^+$ complexes, which are also low-spin (see Table 2).[34] A minor high-spin
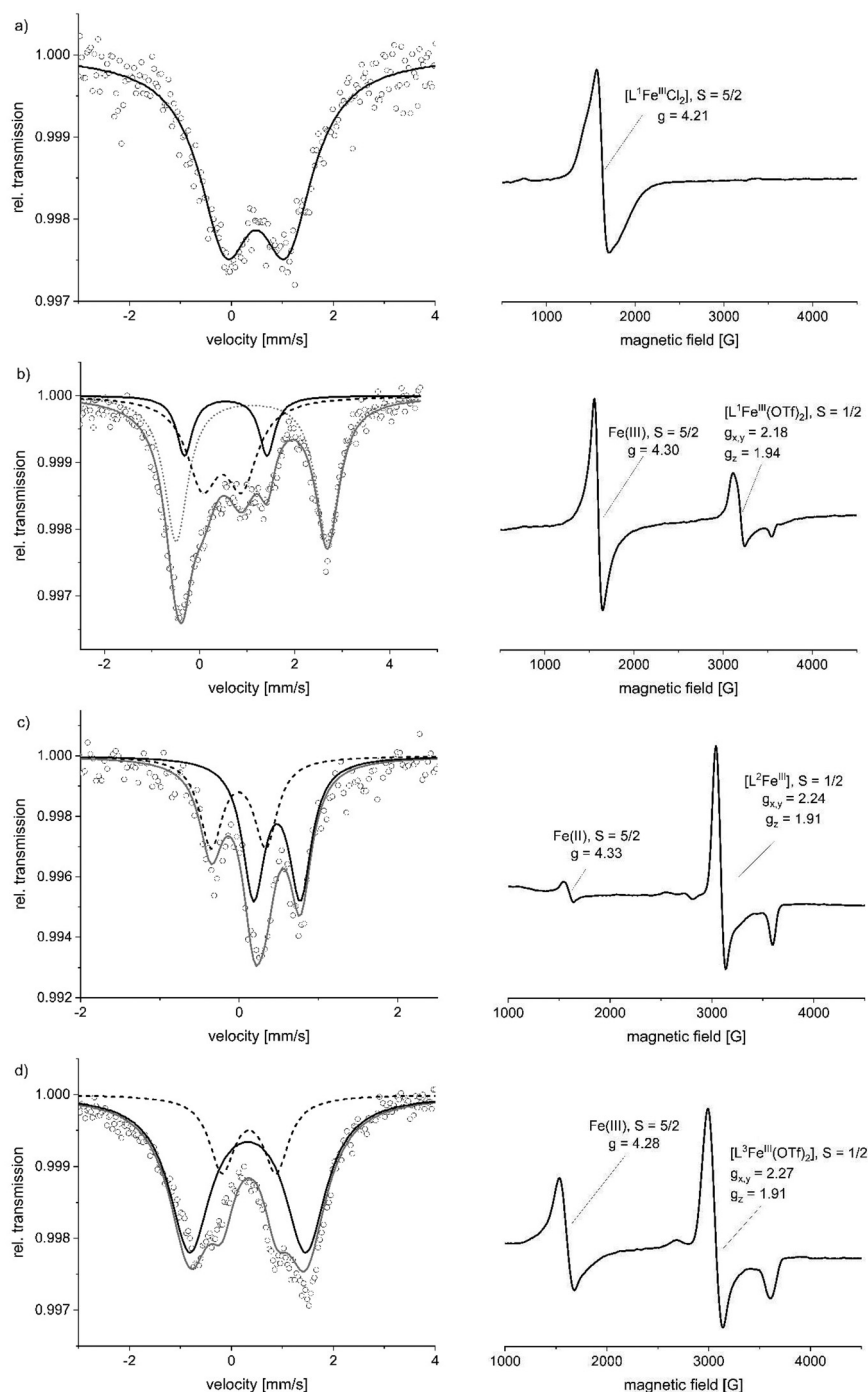
Fig. 4 (a) Mössbauer (left) and EPR measurements (right) of the degradation species of the complex [(L^1)Fe^{IV}=NTs(Cl)](Cl) Mössbauer measurement: δ = 0.48, ΔE_Q = 1.19 mm s^{-1}; [Fe^{II}] 1.0 mM, 2–3 eq. PhINTs, MeCN, 80 K, aged for 10 min at rt before measurement; EPR measurement: f = 9.631378 GHz; aged for 5 h at rt, [Fe^{II}] 2 mM, 2–3 eq. PhINTs, MeCN, 10 K. (b) Mössbauer (left) and EPR measurements (right) of the degradation species of the complex [(L^1)Fe^{IV}=NTs(MeCN)](OTf)$_2$. Mössbauer measurement: black solid line: iron(III) species (1) δ = 0.48, ΔE_Q = 0.83 mm s^{-1}; black dashed line: iron(III) species (2) δ = 0.55, ΔE_Q = 1.74 mm s^{-1}; gray dotted line: iron(II) complex δ = 1.10, ΔE_Q = 3.18 mm s^{-1}; gray solid line: simulated measurement curve. [Fe^{II}] 1.0 mM, 2–3 eq. PhINTs, MeCN, 80 K, aged for 10 min at rt before measurement. EPR measurement: f = 9.633 158 GHz (right). [Fe^{II}] 2 mM, 2–3 eq. PhINTs, MeCN, aged for 5 h at rt before measurement. (c) Mössbauer (left) and EPR measurements (right) of the degradation species of the complex [(L^2)Fe^{IV}=NTs](OTf)$_2$. Mössbauer measurement: black solid line: high-spin iron(III) species δ = 0.48, ΔE_Q = 0.59 mm s^{-1}; black dashed line: iron(IV) species δ = −0.01, ΔE_Q = 0.69 mm s^{-1}; gray line: simulated measurement curve. Aged for 90 min at rt, [Fe^{II}] 1.0 mM, 2–3 eq. PhINTs, MeCN, 80 K. EPR measurement: Aged for 24 h at rt, f = 9.632 442 GHz, [Fe^{II}] 2 mM, 2–3 eq. PhINTs, MeCN, 5–10 K. (d) Mössbauer (left) and EPR measurements (right) of the degradation species of the complex [(L^3)Fe^{IV}=NTs](OTf)$_2$. Mössbauer measurement: black solid line: low-spin iron(III) species δ = 0.32, ΔE_Q = 2.28 mm s^{-1}; black dashed line: high-spin iron(III) species δ = 0.35, ΔE_Q = 1.06 mm s^{-1}; gray line: simulated measurement curve. Aged for 15 min at rt [Fe^{II}] 1.0 mM, 2–3 eq. PhINTs, MeCN, 80 K. EPR measurement: aged for 40 min at rt, f = 9.634 350 GHz, [Fe^{II}] 2 mM, 2–3 eq. PhINTs, MeCN, 5–10 K.

Table 2 Spectroscopic characterization of degradation products derived from bispidine-based iron(IV)–tosylimido complexes and related systems bearing the ligands L^4 and L^5 depicted in Fig. 1

Complex	S	λ [nm] (ε [mol^{-1} cm^{-1}])	δ [mm s^{-1}]	ΔE_Q [mm s^{-1}]	g (xy; z)
$[(L^1_{-H})Fe^{III}-NTs(Cl)]Cl$ (species **A**)	5/2	480	0.48	1.19	4.21
$[(L^1)Fe^{II}(MeCN)_2](OTf)_2$	2	410 (1558)	1.10	3.18	
$[(L^1_{-H})Fe^{III}-NTs(MeCN)](OTf)_2$ (species **A**)	5/2	500	0.48	0.83	4.30
$[(L^1_{-H})Fe^{III}-NTs(MeCN)](OTf)_2$ (species **A**)	1/2				2.18; 1.49
$[(L^1)Fe^{III}(MeCN)_2](OTf)_2$ (species **B**)	5/2		0.55	1.74	
$[(L^2)Fe^{IV}=NTs](OTf)_2$	1	735	−0.01	0.69	
$[(L^2_{-H})Fe^{III}-NTs](OTf)_2$ (species **A**)	5/2	530 (2500)	0.48	0.59	4.33
$[(L^2_{-H})Fe^{III}-NTs](OTf)_2$ (species **A**)	1/2				2.24; 1.91
$[(L^3)Fe^{III}-NHTs](OTf)_2$ (species **D**)	1/2	500	0.32	2.28	2.27; 1.91
$[(L^3)Fe^{III}(MeCN)](OTf)_2$ (species **F**)	5/2		0.35	1.06	4.28
$[(L^4)Fe^{III}-NHTs](OTf)_2$ [34]	1/2	468	0.27	−2.03	2.24; 1.95
$[(L^5)Fe^{III}-NHTs](OTf)_2$ [34]	1/2	472	0.28	2.40	2.23; 1.93

component is detectable, both in the Mössbauer and in the corresponding EPR spectra (Fig. 4d), indicating the presence of a second, structurally distinct iron(III) species. Notably, an additional EPR spectrum recorded five hours after oxidation (see SI Fig. S25) reveals only the high-spin signal, suggesting a time-dependent interconversion. At this point, the UV-vis-NIR spectrum shows no remaining charge-transfer band (see SI Fig. S4), indicating complete loss of the tosylimido-derived functionality. This late-stage species is therefore assigned, by analogy to the triflate L^1 complex, to an iron(III) center lacking any –NTs or –NHTs ligand, likely formed *via* displacement in the course of degradation (species **F**, Scheme 3). Taken together, the data support the formation of a transient $[(L^3)Fe^{III}-NHTs]^{2+}$ species as the dominant early-stage degradation product for $[(L^3)Fe^{IV}=NTs]^{2+}$, followed by slower conversion to a high-spin iron(III) species devoid of the original tosylimido moiety.

Group transfer to styrene

The investigation of the degradation pathways and products of the oxidized bispidine-iron complexes indicates that an active iron(IV)-tosylimido species also has to be present for the complexes with L^1. To further support this assumption, the NTs group transfer capability of the complexes was examined. For this purpose, the tosylimido group transfer onto styrene was studied for the tetradentate bispidine iron complex. In a catalytic reaction, PhINTs was combined with the substrate styrene, followed by the addition of a 5 mM iron(II) solution in MeCN (cat : ox : sub = 1 : 20 : 100, rt, Ar). Upon completion of the reaction, indicated by formation of a clear solution (the limited solubility of the oxidant in MeCN leads to turbidity), both the yield and the approximate duration, and thus a qualitative measure of the reaction rate, were determined. The results are summarized in Table 3. Product formation was observed for all complexes studied, supporting the formation of a reactive tosylimido species for all bispidine-iron complexes. However, differences in yields and TOFs were noted. Both the yield and TOF were significantly higher for the complex with the tetradentate ligand and chloride counter ion, compared to the triflate analogue. $[(L^1)Fe^{IV}=NTs(Cl)](Cl)$ exhi-

Table 3 Yields and TOFs of the catalytic experiments with styrene using bispidine iron complexes. ([Fe^{II}] 5 mM, 20 eq. PhINTs, 100 eq. styrene (cat : ox : substrate 0.05 : 1 : 5), MeCN, Ar, rt)

Complex	Yield [% Ox]	Duration	TOF [h^{-1}]	Lit.
$[(L^1)Fe^{II}Cl_2]$	39.0 (1.4)	64 min	18.5 (0.3)	This work
$[(L^1)Fe^{II}(MeCN)_2]OTf_2$	16.5 (3.3)	21 h 45 min	0.9 (0.5)	This work
$[(L^2)Fe^{II}(MeCN)]OTf_2$	33.5 (1.5)	3 h 13 min	6.3 (3.1)	40
$[(L^3)Fe^{II}(MeCN)]OTf_2$	20.0 (1.2)	36 min	32.9 (2.3)	40

bits more than double the yield and a substantially shorter reaction time. The same trend is observed as in the analogous oxido system: the coordination of a halide accelerates the reaction compared to a coordinated acetonitrile molecule, and this was shown to be due to ligand field dependent spin-state energetics. For tetradentate bispidine-iron(IV)–oxido complexes the triplet-quintet gap is markedly smaller with chloride than with a weakly coordinating ligand, enabling more facile two-state reactivity and faster productive group transfer, and we therefore expect an analogous coligand dependent spin-gap effect for the bispidine-based $Fe^{IV}=NTs$ species as well.[59] Comparing these results with those with the pentadentate ligand systems, it is evident that the yield for $[(L^2)Fe^{IV}=NTs]^{2+}$ is higher than that for $[(L^3)Fe^{IV}=NTs]^{2+}$, but the TOF is lower. The system with L^3 exhibits by far the highest TOF among the bispidine systems investigated here.

Conclusion

This work reveals distinct degradation mechanisms for bispidine–iron(IV)–tosylimido complexes and demonstrates how subtle changes in ligand topology and coordination geometry critically influence the reactivity and stability of these systems. While the tetradentate ligand L^1 and the pentadentate ligand L^2 direct the system toward a shared cyclic degradation pathway involving high-spin $[(L^{1/2}_{-H})Fe^{III}-NTs]^{2+}$ species leading to N-centered demethylation, the L^3 based complex follows an orthogonal route *via* formation of a low-spin $[(L^3)Fe^{III}-NHTs]^{2+}$ species. This mechanistic divergence high-

lights the role of axial *vs.* equatorial tosylimido coordination in governing the fate of reactive intermediates. The indirect identification of the reactive $[(L^1)Fe^{IV}=NTs]^{2+}$ species *via* its degradation products, together with successful NTs group transfer to styrene across all systems studied, provides both mechanistic insight and functional evidence for the tosylimido reactivity of iron complexes. The tosylimido complexes bearing tetradentate ligands display a higher reactivity in comparison to other tosylimido species, consistent with the behavior of their oxido analogues, that they cannot be detected spectroscopically under standard conditions.

Experimental section

Methods and materials

All chemicals and reagents were purchased from commercial sources (ABCR; ACROS, Sigma-Aldrich; TCI). Dry acetonitrile was purified using an MB SPS 5 solvent purification system from MBraun. Air-sensitive materials were prepared and handled using either Schlenk techniques or in a glovebox under Ar atmosphere. The oxidant (*N*-(*p*-toluenesulfonyl) imino)phenyliodinane (PhINTs) was synthesized according to the procedures of Yamada *et al.* and Evans *et al.*, washed with dichloromethane, and stored in a glovebox at −30 °C under argon until its use.[60–62] All Data were analyzed and visualized using OriginPro 2020, unless otherwise stated.

HR ESI-MS experiments were carried out on an ApexQe hybrid 9.4 T FT-ICR from Bruker. Tandem mass experiments were carried out on a timsTOFfleX mass spectrometer from Bruker. For MS and tandem MS measurements samples with iron complex concentrations of 10^{-5} M were prepared. For the investigation of the oxidized iron species, the reactions were carried out under the same conditions as used for the other measurements (in dry MeCN in a glove box under argon), and were diluted accordingly for the MS measurements (details see SI). The measurements were carried out by the Mass Spectrometry Facility, Department of Chemistry, University of Heidelberg, Heidelberg, Germany.

Elemental analyses were performed on a CHN-O Vario EL by the "Mikroanalytisches Labor", Department of Chemistry, Heidelberg University, Heidelberg, Germany.

UV-vis-NIR spectra were recorded on an Agilent 8453 spectrophotometer equipped with an USP-203-A cryostat from Unisoku.

[57]Fe Mössbauer spectra were recorded on an alternating constant-acceleration spectrometer using iron-57 enriched samples. The minimal line-width was 0.24 mm s^{-1} full-width at half-height. The sample temperature was maintained constant in a bath cryostat (Wissel MBBC-HE0106). [57]Co/Rh was used as the radiation source. Isomer shifts were determined relative to α-iron at room temperature.

EPR spectra were recorded on a Bruker ELEXSYS-E500 instrument. The measurements were made in vertical mode at X-band (microwave frequency 9.63461–9.63691 GHz) The spectrometer was equipped with a F-70 Sumitomo cryogenics

helium cryostat, Bruker ER4116-DM resonator, Oxford LLT 650 low loss transfer tube, and an Oxford ITC503 temperature controller. EPR tubes (3 mm, quartz) were filled with 200 μL of sample.

NMR spectra were recorded at 400 MHz (^{1}H) and 101 MHz (^{13}C) on Avance II or at 600 MHz (^{1}H) and 151 MHz (^{13}C) on Avance III instruments from Bruker with the solvent as internal reference.

Product analysis of bulk oxidation reactions. Standard conditions for the reaction with iron(IV)–tosylimido species: In a glove box, a 1.5 ml glass vial was equipped with a stirring bar, 1 eq. of PhINTs (15–20 mg) and 5 eq. of substrate (*ca.* 30 μl styrene). The reaction was started by addition of a 5 mM solution of the Fe^{II} complex (0.1 eq.), dissolved in dry, absolute MeCN. The sequence of substrate addition was chosen to avoid potential side reactions and to ensure that as soon as the tosylimido species is formed, it can react with the substrate. The reaction was stopped after 17 h. For the work-up, the vials were taken out of the glovebox and the solutions were filtered over a silica pipette column to separate the iron catalysts. The columns were washed with 3 ml EtOAc and the combined filtrate was evaporated at 40 °C. The aziridination yields were determined by ^{1}H NMR spectroscopy. Therefore, 1,3,5-trimethoxybenzene (5 to 15 mg – exact amount noted) was added as internal standard to the residue, which was dissolved CD$_2$Cl$_2$. All experiments were performed twice. Yields are with respect to used amount of oxidant.

Preparation of the ligands and complexes

The ligands and iron(II) complexes used were synthesized according to literature known procedures and characterization by NMR, HR ESI-MS and elemental analyses.[63–65]

$[(L^1)Fe^{II}(MeCN)_2]OTf_2$. EA ($C_{27}H_{29}FeF_6N_5O_{11}S_2$) [%]: calc.: C, 38.91; H, 3.51; N, 8.40; exp.: C, 38.70; H, 3.70; N, 8.40. HR ESI-MS (pos., MeCN): m/z = 643.0765 (100%) (calc.: 643.0767) $[Fe^{II}(L^1) + OTf]^+$.

$[(L^1)Fe^{II}Cl_2]$. EA ($C_{25}H_{29}Cl_2FeN_5O_5 \cdot H_2O$) [%]: calc.: C, 48.10; H, 5.01; N, 11.22, exp.: C, 47.98; H, 5.02; N, 10.94. HR ESI-MS (pos., MeCN): m/z = 529.0938 (100%) (calc.: 529.0936) $[Fe^{II}(L^1) + Cl]^+$.

$[(L^2)Fe^{II}(MeCN)]OTf_2$. EA ($C_{32}H_{32}FeF_6N_6O_{11}S_2 \cdot 2H_2O$) [%]: calc.: C, 40.60; H, 3.83; N, 8.88; exp.: C, 40.80; H, 3.89; N, 8.59. HR ESI-MS (pos., MeCN): m/z = 720.1030 (100%) (calc.: 720.1033) $[Fe^{II}(L^2) + OTf]^+$.

$[(L^3)Fe^{II}(MeCN)]OTf_2$. EA ($C_{32}H_{32}FeF_6N_6O_{11}S_2 \cdot 2H_2O$) [%]: calc.: C, 40.60; H, 3.83; N, 8.88; exp.: C, 40.65; H, 3.74; N, 8.31. HR ESI-MS (pos., MeCN): m/z = 606.1190 (99%) (calc.: 606.1201) $[Fe^{II}(L^3) + Cl]^+$, m/z = 624.1295 (100%) (calc.: 624.1307) $[Fe^{II}(L^3) + Cl + H_2O]^+$.

$[(L^1)^{57}Fe^{II}(MeCN)_2]OTf_2$. EA ($C_{25}H_{28}FeF_6N_4O_{12}S_2 \cdot 0.5$ MeCN) [%]: calc.: C, 37.53; H, 3.57; N, 7.58, exp.: C, 37.37; H, 3.58; N, 7.69. HR ESI-MS (pos., MeCN/MeOH): m/z = 526.1436 (61%) (calc.: 526.1435) $[^{57}Fe^{II}(L^1) + OMe]^+$, m/z = 644.0772 (100%) (calc.: 644.0773) $[^{57}Fe^{II}(L^1) + OTf]^+$.

$[(L^1)^{57}Fe^{II}Cl_2]$. EA ($C_{23}H_{28}Cl_2FeN_4O_6 \cdot 0.75$ MeCN) [%]: calc.: C, 47.84; H, 4.96; N, 10.82, exp.: C, 47.90; H, 4.89; N, 10.75. HR

ESI-MS (pos., MeCN/MeOH): m/z = 530.0941 (61%) (calc.: 530.0940) $[^{57}Fe^{II}(L^1) + Cl]^+$, m/z = 562.1203 (100%) (calc.: 562.1202) $[^{57}Fe^{II}(L^1) + Cl + MeOH]^+$.

$[(L^2)^{57}Fe^{II}(MeCN)]OTf_2$. EA ($C_{32}H_{32}FeF_6N_6O_{11}S_2$·MeOH· $0.5H_2O$) [%]: calc.: C, 41.60; H, 3.91; N, 8.82; exp.: C, 41.67; H, 3.97; N, 8.74. HR ESI-MS (pos., MeCN): m/z = 721.1038 (100%) (calc.: 721.1037) $[Fe^{II}(L^2) + OTf]^+$.

$[(L^3)^{57}Fe^{II}(MeCN)]OTf_2$. EA ($C_{30}H_{31}FeF_6N_5O_{12}S_2$·0.25MeCN· $0.5H_2O$) [%]: calc.: C, 40.35; H, 3.64; N, 8.10; exp.: C, 40.38; H, 3.72; N, 8.06. HR ESI-MS (pos., MeCN): m/z = 607.1207 (100%) (calc.: 607.1206) $[Fe^{II}(L^3) + Cl]^+$.

Author contributions

The manuscript was written through contributions of all authors. All authors have given approval to the final version of the manuscript. K. B. prepared the original draft and performed MS and EPR measurements and experiments regarding the iron(IV)– oxido complexes. T. J. contributed to data visualization, writing through review and editing, and carried out major parts of the investigation, including UV-vis-NIR, MS, and EPR measurements as well as sample preparation for Mössbauer spectroscopy. F. R. performed the Mössbauer measurements. T. G. provided resources and contributed to writing through review and editing. P. C. provided resources, supervision, and contributed to writing through review and editing.

Conflicts of interest

There are no conflicts to declare.

Data availability

Supplementary information (SI): protocols for sample preparation, MS data, aziridination experiments, EPR spectra, and UV/Vis-NIR spectra. See DOI: https://doi.org/10.1039/d5dt02063h.

Raw data are stored on the university servers and can be accessed *via* the corresponding author if necessary.

Acknowledgements

References

1 G. Coin and J. M. Latour, *J. Inorg. Biochem.*, 2021, **225**, 111613.

2 K. Ray, F. F. Pfaff, B. Wang and W. Nam, *J. Am. Chem. Soc.*, 2014, **136**, 13942–13958.

3 X. Engelmann, I. Monte-Pérez and K. Ray, *Angew. Chem., Int. Ed.*, 2016, **55**, 7632–7649.

4 M. N. Cosio and D. C. Powers, *Nat. Rev. Chem.*, 2023, **7**, 424–438.

5 M. Guo, T. Corona, K. Ray and W. Nam, *ACS Cent. Sci.*, 2019, **5**, 13–28.

6 J. Hohenberger, K. Ray and K. Meyer, *Nat. Commun.*, 2012, **3**, 720.

7 C. Krebs, D. G. Fujimori, C. T. Walsh and J. M. Bollinger Jr., *Acc. Chem. Res.*, 2007, 484–492.

8 M. M. Abu-Omar, A. Loaiza and N. Hontzeas, *Chem. Rev.*, 2005, **105**, 2227–2252.

9 A. R. McDonald and L. Que, *Coord. Chem. Rev.*, 2013, **257**, 414–428.

10 W. Nam, *Acc. Chem. Res.*, 2015, **48**, 2415–2423.

11 E. I. Solomon, K. M. Light, L. V. Liu, M. Srnec and S. D. Wong, *Acc. Chem. Res.*, 2013, **46**, 2725–2739.

12 W. Nam, Y. M. Lee and S. Fukuzumi, *Acc. Chem. Res.*, 2014, **47**, 1146–1154.

13 F. Avenier and J. M. Latour, *Chem. Commun.*, 2004, **4**, 1544– 1545.

14 M. P. Jensen, M. P. Mehn and L. Que, *Angew. Chem., Int. Ed.*, 2003, **42**, 4357–4360.

15 C. A. Grapperhaus, B. Mienert, E. Bill, T. Weyhermu and K. Wieghardt, *Inorg. Chem.*, 2000, **39**, 5306–5317.

16 X. Li, L. Dong and Y. Liu, *Inorg. Chem.*, 2020, **59**, 1622–1632.

17 N. W. Goldberg, A. M. Knight, R. K. Zhang and F. H. Arnold, *J. Am. Chem. Soc.*, 2019, **141**, 19585–19588.

18 S. Hong, K. D. Sutherlin, A. K. Vardhaman, J. J. Yan, S. Park, Y. M. Lee, S. Jang, X. Lu, T. Ohta, T. Ogura, E. I. Solomon and W. Nam, *J. Am. Chem. Soc.*, 2017, **139**, 8800–8803.

19 P. Müller and C. Fruit, *Chem. Rev.*, 2003, **103**, 2905–2919.

20 P. F. Kuijpers, J. I. van der Vlugt, S. Schneider and B. de Bruin, *Chem. – Eur. J.*, 2017, **23**, 13819–13829.

21 G. Dequirez, V. Pons and P. Dauban, *Angew. Chem., Int. Ed.*, 2012, **51**, 7384–7395.

22 E. Vitaku, D. T. Smith and J. T. Njardarson, *J. Med. Chem.*, 2014, **57**, 10257–10274.

23 S. D. Roughley and A. M. Jordan, *J. Med. Chem.*, 2011, **54**, 3451–3479.

24 J. Castro, X. Westworth, R. Shrestha, K. Yokoyama and Z. Guan, *Adv. Mater.*, 2024, **36**, 1–7.

25 F. Thomas, M. Oster, F. Schön, K. C. Göbgen, B. Amarouch, D. Steden and A. Hoffmann, *Dalton Trans.*, 2021, **50**, 6444– 6462.

26 Y. Ren, J. Forté, K. Cheaib, N. Vanthuyne, L. Fensterbank, H. Vezin, M. Orio, S. Blanchard and M. Desage-El Murr, *iScience*, 2020, **23**(3), 100955.

27 K. Bleher, P. Comba, M. Gast, S. Kronenberger and T. Josephy, *Inorg. Chim. Acta*, 2022, **532**, 120752.

28 P. Comba, M. Merz and H. Pritzkow, *Eur. J. Inorg. Chem.*, 2003, 1711–1718.

29 P. Comba, C. Lang, C. L. De Laorden, A. Muruganantham, G. Rajaraman, H. Wadepohl and M. Zajaczkowski, *Chem. – Eur. J.*, 2008, **14**, 5313–5328.

30 J. A. Halfen, J. M. Uhan, D. C. Fox, M. P. Mehn and L. Que, *Inorg. Chem.*, 2000, **39**, 4913–4920.

31 T. Josephy, M. Heiduk, T. Saxl and K. Bleher, *Inorg. Chim. Acta*, 2025, 122587.

32 V. Bagchi, A. Kalra, P. Das, P. Paraskevopoulou, S. Gorla, L. Ai, Q. Wang, S. Mohapatra, A. Choudhury, Z. Sun, T. R. Cundari and P. Stavropoulos, *ACS Catal.*, 2018, **8**, 9183–9206.

33 H. Nishikori, C. Ohta, E. Oberlin, R. Irie and T. Katsuki, *Tetrahedron*, 1999, **55**, 13937–13946.

34 G. Sabenya, I. Gamba, L. Gómez, M. Clémancey, J. R. Frisch, E. J. Klinker, G. Blondin, S. Torelli, L. Que, V. Martin-Diaconescu, J. M. Latour, J. Lloret-Fillol and M. Costas, *Chem. Sci.*, 2019, **10**, 9513–9529.

35 E. J. Klinker, T. A. Jackson, M. P. Jensen, A. Stubna, G. Juhász, E. L. Bominaar, E. Münck and L. Que, *Angew. Chem., Int. Ed.*, 2006, **45**, 7394–7397.

36 S. Kumar, A. S. Faponle, P. Barman, A. K. Vardhaman, C. V. Sastri, D. Kumar and S. P. De Visser, *J. Am. Chem. Soc.*, 2014, **136**, 17102–17115.

37 A. K. Vardhaman, P. Barman, S. Kumar, C. V. Sastri, D. Kumar and S. P. De Visser, *Angew. Chem., Int. Ed.*, 2013, **52**, 12288–12292.

38 G. Mukherjee, F. G. C. Reinhard, U. K. Bagha, C. V. Sastri and S. P. de Visser, *Dalton Trans.*, 2020, **49**, 5921–5931.

39 K. Bleher, P. Cieslik and P. Comba, *Dalton Trans.*, 2025, **54**, 4405.

40 T. Josephy, R. Kumar, K. Bleher, F. Röhs, T. Glaser, G. Rajaraman and P. Comba, *Inorg. Chem.*, 2024, **63**, 12109–12119.

41 M. Abu-Odeh, K. Bleher, N. J. Britto, P. Comba, M. Gast, M. Jaccob, M. Kerscher, S. Krieg and M. Kurth, *Chem. – Eur. J.*, 2021, **27**, 11377–11390.

42 J. England, Y. Guo, E. R. Farquhar, V. G. Young, E. Münck and L. Que, *J. Am. Chem. Soc.*, 2010, **132**, 8635–8644.

43 A. Nielsen, F. B. Larsen, A. D. Bond and C. J. McKenzie, *Angew. Chem., Int. Ed.*, 2006, **45**, 1602–1606.

44 X. Lu, X. X. Li, Y. M. Lee, Y. Jang, M. S. Seo, S. Hong, K. Bin Cho, S. Fukuzumi and W. Nam, *J. Am. Chem. Soc.*, 2020, **142**, 3891–3904.

45 Y. Liu, X. Guan, E. L. M. Wong, P. Liu, J. S. Huang and C. M. Che, *J. Am. Chem. Soc.*, 2013, **135**, 7194–7204.

46 A. Decker, J. U. Rohde, L. Que and E. I. Solomon, *J. Am. Chem. Soc.*, 2004, **126**, 5378–5379.

47 E. Gouré, D. Senthilnathan, G. Coin, F. Albrieux, F. Avenier, P. Dubourdeaux, C. Lebrun, P. Maldivi and J. M. Latour, *Angew. Chem., Int. Ed.*, 2017, **56**, 4305–4309.

48 X. X. Li, X. Lu, J. W. Park, K. Bin Cho and W. Nam, *Chem. – Eur. J.*, 2021, **27**, 17495–17503.

49 X. Lu, X. X. Li, M. S. Seo, Y. M. Lee, M. Clémancey, P. Maldivi, J. M. Latour, R. Sarangi, S. Fukuzumi and W. Nam, *J. Am. Chem. Soc.*, 2019, **141**, 80–83.

50 P. Comba, B. Pokrandt and H. Wadepohl, *Aust. J. Chem.*, 2017, **70**, 576–580.

51 K. Bleher, P. Comba, J. H. Gross and T. Josephy, *Dalton Trans.*, 2022, **51**, 8625–8639.

52 R. L. Lucas, D. R. Powell and A. S. Borovik, *J. Am. Chem. Soc.*, 2005, **127**, 11596–11597.

53 J. H. Gross, *Mass Spectrometry*, Springer Nature, 3rd edn, 2017.

54 C. J. Conder, H. Jawale and P. G. Wenthold, *Mass Spectrom. Rev.*, 2023, **42**, 1604–1624.

55 M. H. Studier and E. J. Hart, *J. Am. Chem. Soc.*, 1969, **91**, 4068–4072.

56 B. D. Michael and E. J. Hart, *J. Phys. Chem.*, 1970, **74**, 2878–2884.

57 P. Comba, S. Fukuzumi, C. Koke, B. Martin, A. M. Löhr and J. Straub, *Angew. Chem., Int. Ed.*, 2016, **55**, 11129–11133.

58 J. Bautz, P. Comba and L. Que Jr., *Inorg. Chem.*, 2006, **45**(18), 7077–7082.

59 P. Comba, G. Nunn, F. Scherz and P. H. Walton, *Faraday Discuss.*, 2021, **234**, 232–244.

60 D. A. Evans, M. M. Faul and M. T. Bilodeau, *J. Org. Chem.*, 1991, **56**, 6744–6746.

61 D. A. Evans, M. M. Paul and M. T. Bilodeau, *J. Am. Chem. Soc.*, 1994, **116**, 2742–2753.

62 Y. Yamada, T. Yamamoto and M. Okawara, *Chem. Lett.*, 1975, 361–362.

63 H. Börzel, P. Comba, K. S. Hagen, Y. D. Lampeka, A. Lienke, G. Linti, M. Merz, H. Pritzkow and L. V. Tsymbal, *Inorg. Chim. Acta*, 2002, **337**, 407–419.

64 C. Mannich and P. Mohs, *Ber. Dtsch. Chem. Ges.*, 1930, **63**, 608–612.

65 P. Comba, M. Kerscher and W. Schiek, *Prog. Inorg. Chem.*, 2007, **55**, 613–704.